nature geoscience

Article

https://doi.org/10.1038/s41561-023-01185-4

Calabrian forearc uplift paced by slabmantle interactions during subduction retreat

Received: 7 April 2022

Accepted: 19 April 2023

Published online: 01 June 2023



Check for updates

Sean F. Gallen ¹□, Nikki M. Seymour ^{2,3,4}, Christoph Glotzbach ⁵, Daniel F. Stockli⁶ & Paul O'Sullivan ® 7

Evidence from landscape evolution may provide critical constraints for past geodynamic processes, but has been limited by the large uncertainties of topographic reconstructions. Here we present continuous 30-million-year rock uplift histories for three catchments in the Calabrian forearc of southern Italy, using a data-driven inversion of tectonic geomorphology measurements. We find that rock uplift rates were high (>1 mm yr⁻¹) from about 30 to 25 million years ago (Ma) and progressively declined to <0.4 mm yr⁻¹ by ~15 Ma, then remained low before abruptly increasing around 1.5–1.0 Ma. These uplift rates do not match the forearc's subduction velocity record, implying that uplift was not dominated by crustal thickening due to subduction-driven sediment influx. Through comparisons with slab descent reconstructions, we instead argue that the forearc uplift history primarily reflects the progressive establishment and abrupt destruction of an upper-mantle convection cell with strong negative buoyancy. We suggest that the convection cell vigour increased as the slab-induced mantle flow field began to interact with the 660-km mantle transition zone, causing uplift rates to decline from 25 to 15 Ma. Then, once the slab encountered the transition zone, the fully established convection cell subdued uplift rates, before being disrupted by slab fragmentation in the Quaternary, driving rapid forearc uplift.

Orogenesis and topographic development in subduction forearcs reflect the integrated effects of numerous processes, including crustal dynamics, megathrust strength and slab-mantle interactions¹⁻³. Although the principles of how crustal processes and changes in megathrust strength affect forearc orogenesis are generally understood in the context of accretionary wedge dynamics^{1,3-6}, the potentially important role of slab-mantle interactions remains poorly constrained in natural settings^{2,7–10}. Numerical and analogue modelling studies indicate that slab-mantle interactions affect mountain building and drive topographic change throughout the lifetime of subduction¹¹⁻¹³. Slab tearing and small-scale mantle flow around torn slab segments $can also \, affect \, for earc \, or ogens is ^{2,14}. \, However, we \, are \, currently \, limited \,$ in our ability to reconstruct the long-term topographic and rock uplift histories required to test model predictions in nature.

We overcome these difficulties by leveraging advances in our ability to invert tectonic geomorphology measurements for long-term rock uplift histories 15,16 and apply these techniques to the forearc above the $Calabrian \, subduction \, zone, a \, classic \, example \, of \, a \, retreating \, subduction \,$

Department of Geosciences, Colorado State University, Fort Collins, CO, USA. Department of Geological Sciences, Stanford University, Stanford, CA, USA. 3Department of Earth and Planetary Sciences, University of California Santa Cruz, Santa Cruz, CA, USA. 4Department of Geology, Occidental College, Los Angeles, CA, USA. 5Department of Geosciences, University of Tübingen, Tübingen, Germany. 6Department of Geological Sciences, University of Texas at Austin, Austin, TX, USA. 7GeoSep Services, Moscow, ID, USA. e-mail: sean.gallen@colostate.edu

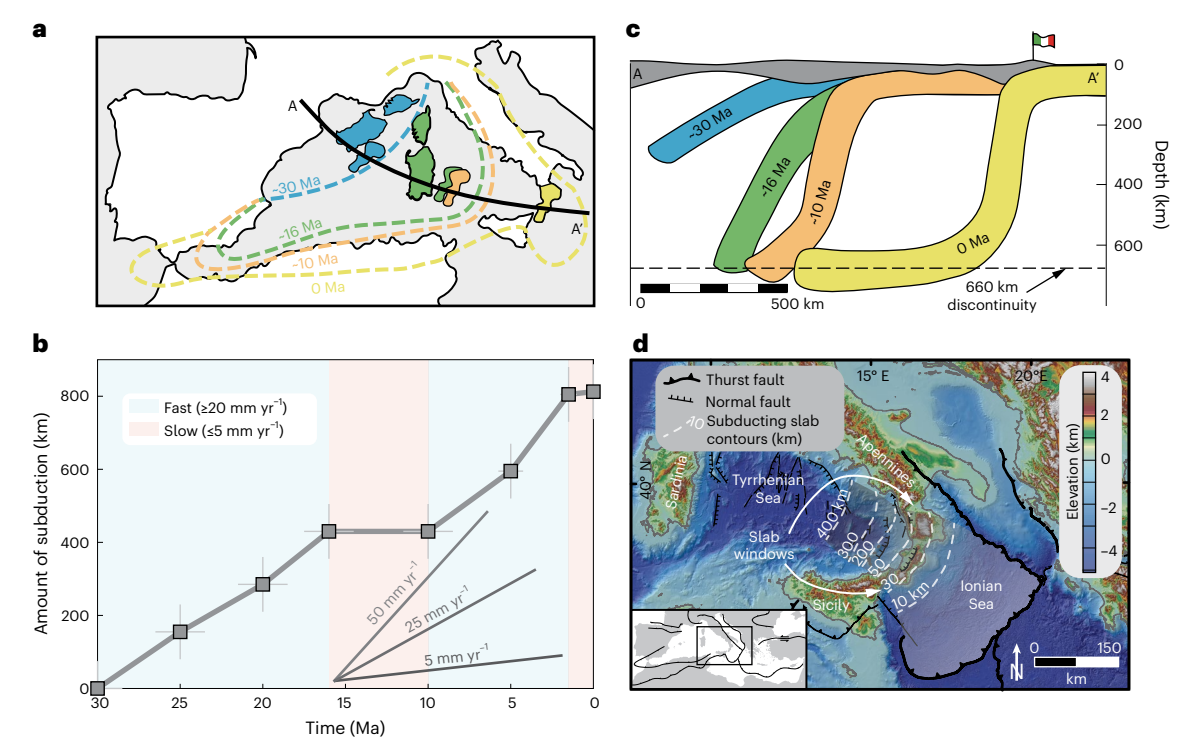


Fig. 1| **Subduction history and regional setting. a**, Retreat history of the Calabrian subduction zone (approximate trench locations are denoted by dashed lines) since -30 Ma (after refs. 17,18,49). **b**, Calabrian subduction history, showing mean subduction amounts with $\pm 1\sigma$ uncertainties (thin grey lines) associated with uncertainties in the subduction history reconstruction (data modified from

refs. 17,18,49). \mathbf{c} , Reconstructions of the location of the subducting slab based on ref. 17. The location of the transect is shown in \mathbf{a} . \mathbf{d} , The contemporary tectonic setting of southern Italy shows some of the major active faults, the modern slab position and depth, and topography and bathymetry. Faults and slab contours are from data provided in ref. 50.

system. We selected Calabria because it has a well-constrained subduction velocity history and slab descent reconstructions from the mid-Cenozoic to the present ^{17,18} (Fig. 1). We use a suite of tectonic geomorphology measurements—low-temperature thermochronometry, cosmogenic radionuclides, marine terraces and fluvial topography—to invert for uplift histories for bedrock catchments from the three main massifs in Calabria. Our results show that changes in rock uplift align with the timing of slab—mantle interactions and slab tearing, suggesting strong geodynamic controls on forearc orogenesis. These findings improve understanding of the geodynamic processes that have affected the Italian peninsula and provide generalizable insight into the dynamics of forearc mountain building.

The Calabrian subduction system

The Calabrian subduction zone is a retreating plate boundary and is an ideal case study to assess the roles of crustal and mantle processes in driving orogenesis (Fig. 1). Being trenchward of the volcanic arc, crustal thickening due to magmatism can be ignored. Calabria is at the leading front of the subduction wedge and can be treated as an accretionary system where forearc crustal thickening is largely a function of accretionary flux (that is, the product of the sediment thickness entering the trench and the subduction velocity).

Calabria records an unsteady translation history across the Western Mediterranean in response to the southeast-directed retreat since rifting off Iberia in the Oligocene^{17,19,20} (Fig. 1a-c). The record shows periods of rapid retreat at 30–16 Ma and 10–2 Ma, when the subduction velocity was -25–60 mm yr⁻¹, and intervening periods at -16–10 Ma and -2–0 Ma when it was an order of magnitude slower (Fig. 1a,b). The decline in rate from -16 to 10 Ma occurred when the subducting slab encountered and draped over the 660-km mantle transition zone^{17,21} (Fig. 1a–c). Slowing at -2–0 Ma is associated with slab–mantle

interactions and small-scale plate reorganizations 18,22 . Late in this history, the subducting Ionian lithosphere tore and fragmented, giving rise to the narrow subduction zone flanked by slab windows observed today (Fig. 1d).

Calabria, and other parts of Italy, record a change in rock uplift and exhumation rates at -2-1 Ma (refs. 15,23-27). High-elevation, low-relief relict topography, as well as marine terraces, document a recent increase in rock uplift rate^{15,23,24,26} (Fig. 2). The forearc uplift history preceding -2 Ma is poorly constrained. Limited existing studies suggest a rapid pulse of exhumation for portions of Calabria from the Oligocene until the Early to Middle Miocene^{15,28}. Uplift rates then declined to bevel the relict topography before increasing to modern values of -0.5-1 mm yr⁻¹ at -2-1 Ma (refs. 15,23,24,26).

Constraining a 30-Myr history of forearc rock uplift

We combine data presented in this study and previously published 28 low-temperature thermochronology (apatite fission track (AFT) and apatite (U-Th)/He (AHe)), 10 Be-derived basin average erosion rates 26,29,30 , coastal marine terraces $^{31-36}$ and fluvial topography to derive continuous 30-Myr rock uplift histories for moderately sized bedrock catchments (-90–150 km²) in the three primary massifs in the Calabrian forearc: Sila, Serre and Aspromonte (Fig. 2). We focus on the catchment scale to simplify the analysis. By selecting moderately sized catchments not cut by major faults, we can assume that spatial variations in rock uplift are negligible, allowing us to focus on temporal changes. Furthermore, this ensures that we work with bedrock rivers in similar geology, which is important for modelling assumptions (Fig. 2).

We use previously published AFT and ¹⁰Be measurements in Sila, our AFT and AHe data in Serre and Aspromonte, and transient river profiles extracted from a 30-m digital elevation model (DEM)

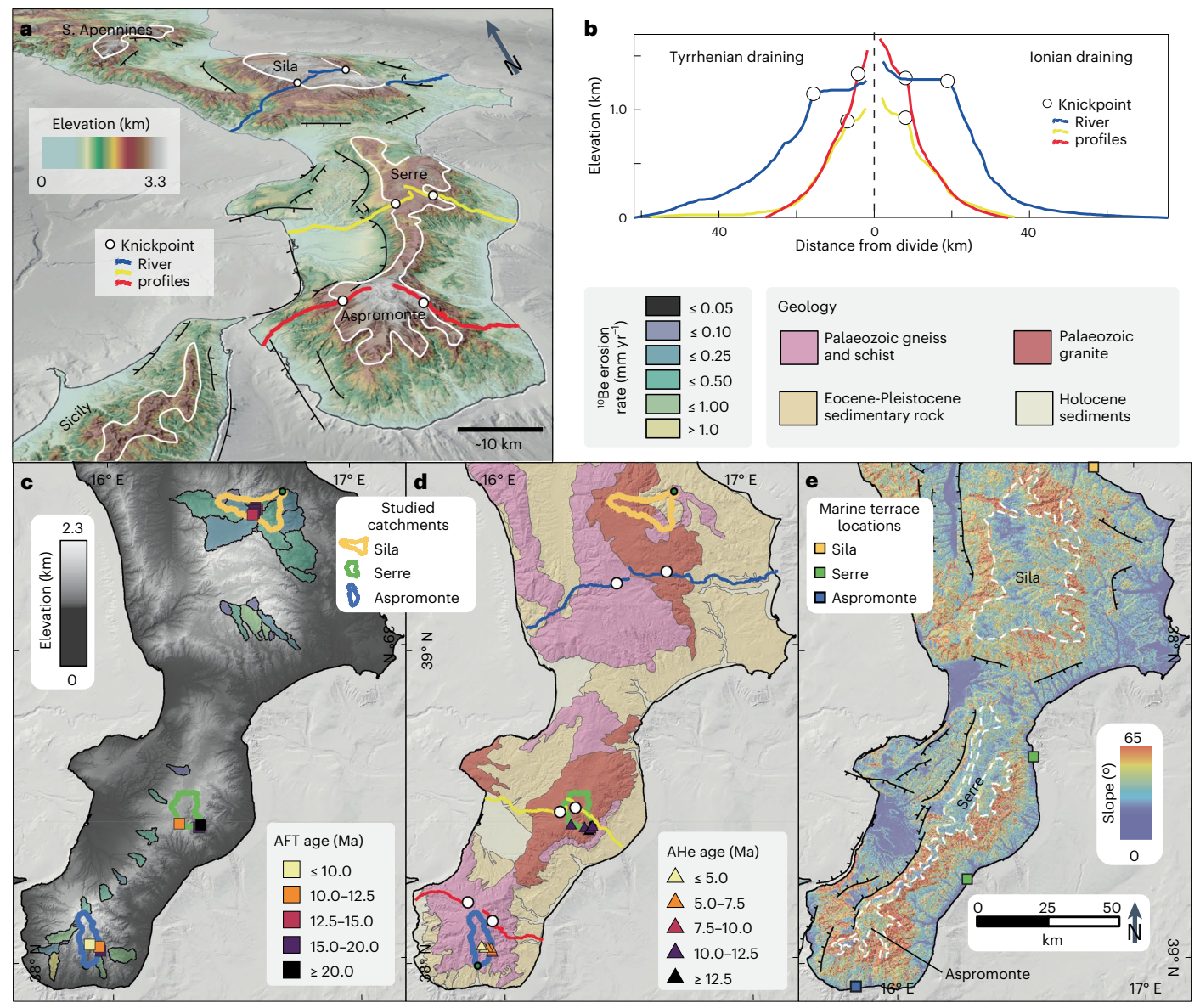


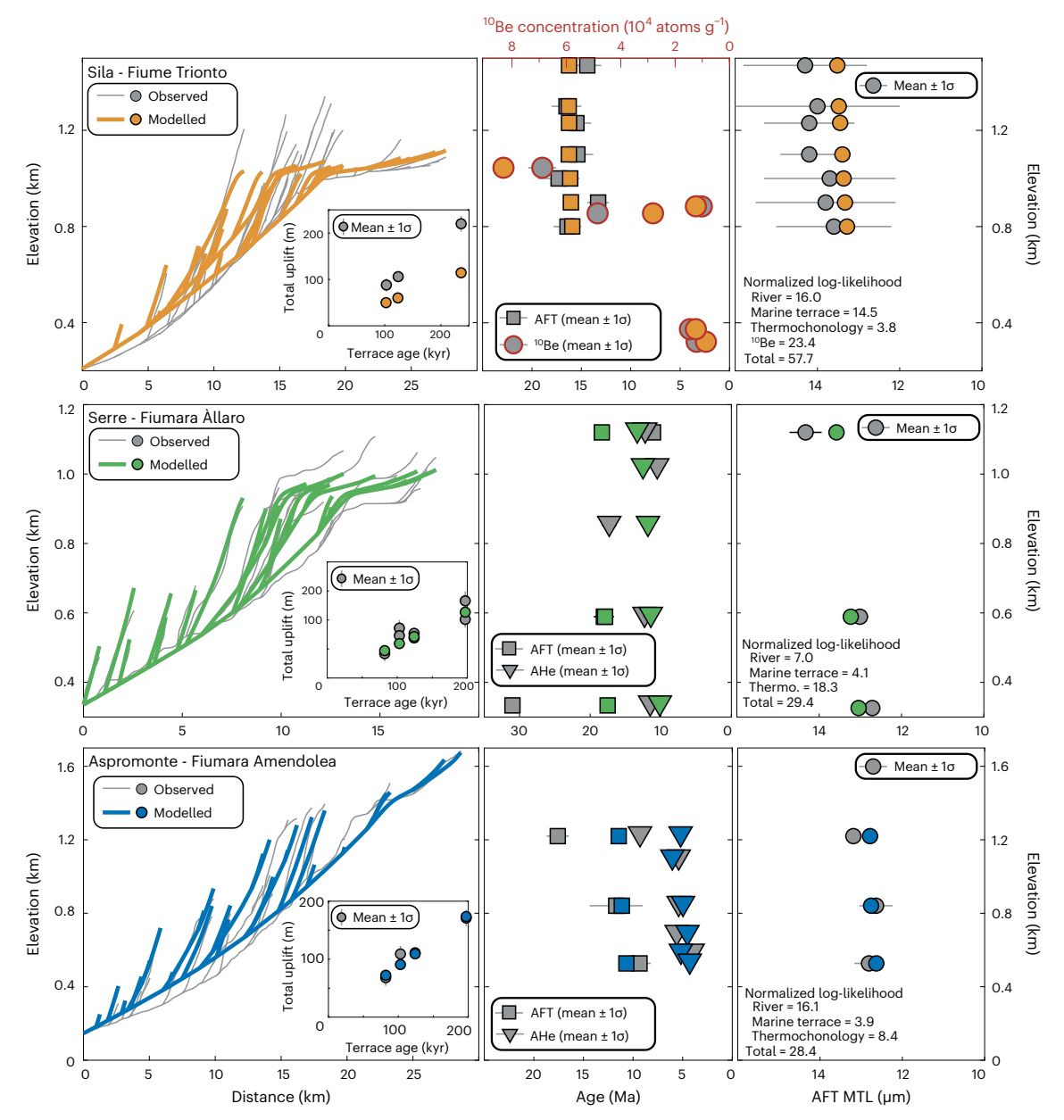
Fig. 2 | Topography, geomorphology and geology of the Calabrian forearc. a, Oblique view of Calabria highlighting the relict topography (white polygons) and the location of the selected transient river profiles shown in ${\bf b}$. ${\bf b}$. Select transient river profiles showing the knickpoints that bound the relict topography. These rivers were selected to highlight that knickpoints exist at -1-km elevation for rivers draining in either direction. ${\bf c}$, Shaded relief map with previously published $^{10}{\rm Be}$

basin average erosion rates 26,2930 and AFT data 28 . **d**, Simplified geologic map 30 along with the location of the river profile shown in **a** and **b** and the AHe dates. The orange, green and blue outlined polygons show the locations of the study catchments in Sila, Serre and Aspromonte, respectively. **e**, Slope map of the Calabrian forearc with some of the active faults (black lines), the relict topography (dashed white polygons) and the marine terrace locations $^{3l-36}$.

and coastal marine terraces near each catchment for our inversion (Fig. 2, Source Data Fig. 2a,d and Supplementary Tables 1–3). AFT ages are ~30–10 Ma and show typically scattered single-age distributions and mean age-elevation trends consistent with a period of rapid cooling in the Oligocene followed by slow cooling around the partial annealing zone^{15,28} (Figs. 2c and 3). AHe ages are ~17–10 Ma in Serre and ~10–4 Ma in Aspromonte, with both sites having positive age-elevation trends consistent with more recent rapid cooling (Figs. 2d and 3). The transient river profiles indicate a period of slow rock uplift, followed by an acceleration to produce the knickpoints and steepened lower profile segments (Figs. 2b and 3). In Sila, ¹⁰Be concentrations decrease below knickpoints, consistent with slow erosion above and more rapid erosion below the knickpoints. Mid-to-late Pleistocene marine terraces indicate modern rock uplift rates between ~0.5 and 1.0 mm yr⁻¹ (refs. 31–36; Figs. 2e and 3).

We invert these datasets using a data-driven Bayesian framework ¹⁵. This approach provides a unified method to derive continuous, long-term rock uplift histories that can achieve a level of precision beyond one data type alone. The thermochronometric measurements determine the older parts of the uplift history, and ¹⁰Be and marine terrace data constrain the more recent uplift history. The river profile data bridge this gap, recording the transition from slow to fast rock uplift rates expressed as high-elevation, low-relief relict topography bound by fluvial knickpoints found at -1-km elevation ^{24–27} (Fig. 2).

The inversion uses a series of forward models to predict the data for an input rock uplift history. The topographic and erosional evolution is determined for a given rock uplift history with the detachment-limited stream power model, which is appropriate for bedrock channels, and simulates the river incision rate, \boldsymbol{E} , as



 $\label{fig:seminor} \textbf{Fig. 3} | \textbf{Best-fit models of the tectonic geomorphology data.} \text{ The maximum a posteriori (MAP) or 'best-fit' results for the three study catchments. The river profiles are shown in the left column, with the marine terrace results shown in the inset. The uncertainties in the marine terrace rock uplift calculations are derived from a Monte Carlo routine that incorporates the uncertainties of all measurements involved (for example, measured elevation, sea-level elevation and terrace age; see Methods for more details). The analytical data are displayed$

in the two right columns. The uncertainties for the 10 Be concentrations and AFT and AHe ages represent the analytical uncertainties. The AFT mean track length (MTL) uncertainties are associated with the standard deviation of the track length measurements for each sample. The text at the bottom of the rightmost columns shows the normalized log-likelihood, which is a measure of the fit quality normalized to the number of data points.

$$E = KA^m S^n \tag{1}$$

where A and S are the upstream drainage area (a proxy for discharge) and local channel slope, respectively, K is an erodibility constant, and m and n are positive constants that reflect the basin hydrology, channel hydraulic scaling and incision process $^{37-39}$. The uplift, erosion and topographic history are then used to drive (1) thermal and kinetic models that predict AFT and AHe data, (2) cosmogenic production and attenuation models that determine 10 Be concentrations and (3) the recent rock uplift history to compare to marine terrace-derived rock uplift measurements. We invert the observed data using the neighbourhood algorithm 40 to determine the acceptable range of stream power parameters and the rock uplift history.

The basic concept is to run a series of forward models that predict the observed data and compare the modelled and observed data via a misfit function, here a Gaussian log-likelihood function. Iterative selection of the next suite of parameters is guided by the prior probability distributions, or more simply the priors, of model parameters, the transitional probability to a new position in the parameter space, and the quality of the model fit. This procedure was repeated -70,000 times for each catchment, and the upper 50th percentile of 'best-fit' models was used to populate the posterior probability distributions of unknown parameters (Methods). However, the posteriors are not very sensitive to the likelihood threshold. We solve for ten free parameters—the three stream power parameters (*K*, *m*, and *n*) and a four-stage

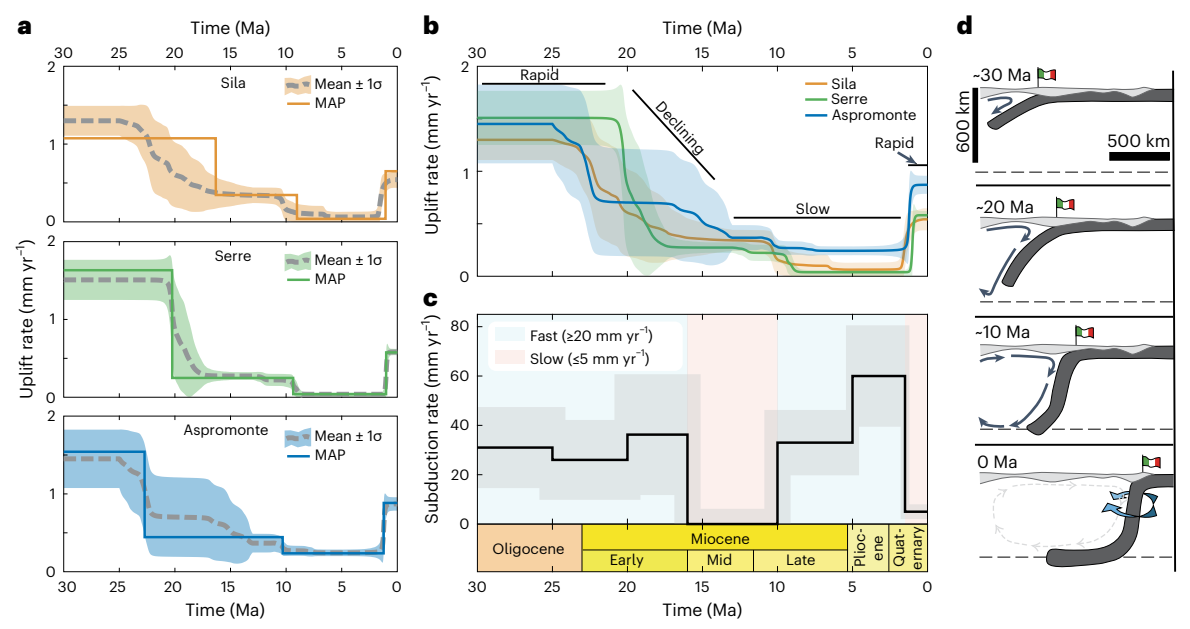


Fig. 4 | **Rock uplift, subduction rate and slab descent histories of the Calabrian subduction system. a**, Rock uplift histories show the three studied catchments. Solid coloured lines show the MAP ('best-fit') results. Grey dashed lines and shaded polygons show the mean $\pm 1\sigma$ uplift histories from the model ensemble. **b**, Mean (thin solid line) $\pm 1\sigma$ (shaded) uplift histories for each catchment. **c**, Subduction rate history of Calabria determined by taking the derivative of the subduction history modified after refs. 17,18,49 in Fig. 1b and

using a Monte Carlo routine to propagate uncertainties. \mathbf{d} , Slab descent history modified after refs. 17,49 to show even 10-Myr increments and interpreted slab mantle interactions. As the slab descends, an upper-mantle convection cell (black line with arrow) grows in size and, upon interacting with the 660-km mantle transition zone (dashed black line), strengthens. During the Quaternary, slab tearing, and lateral mantle flow, the torn slab edges disrupt the upper-mantle convection cell beneath the upper plate.

uplift history (that is, the uplift rates (n=4) and the timing of uplift rate transitions (n=3)). The priors are a uniform range (that is, naïve priors), determined by knowledge of the regional geology and geomorphology. Extended Data Table 1 lists the free parameters, priors and explanations for the prior ranges.

Inversion results and long-term uplift history

The modelled river profile residuals are typically several tens of metres, and knickpoints are predicted at the correct locations (Fig. 3). The modelled marine terrace rock uplift is consistent with the observations in Aspromonte and Serre and slightly underpredicted in Sila due to trade-offs with the ¹⁰Be data (Fig. 3). The ¹⁰Be and AHe fits are better than the noisier AFT data, but the model predicts mean AFT age trends and matches the generally unimodal AFT track length distributions, consistent with the monotonic cooling assumed in the model (Fig. 3).

The posteriors for most parameters are roughly Gaussian distributions (Extended Data Figs. 1–3). The stream power parameters are consistent with typical values 15,26,38,41 (Fig. 3 and Extended Data Figs. 1–4). The m to n ratio is between \sim 0.35 and 0.43, and the n value ranges between \sim 1.05 and 1.40 at all sites. The erodibility constant covaries with these parameters and lies between \sim 1 \times 10⁻⁵ and 1 \times 10⁻⁶ m^{1-2m} yr⁻¹.

The uplift histories are similar among all three catchments (Fig. 4a,b). The initial phase is rapid, -1.2–1.9 mm yr⁻¹, at all sites and slows to -0.2–0.45 mm yr⁻¹ by the Middle Miocene (Fig. 4 and Extended Data Figs. 1–3). The timing of this transition is not well defined, partly because the AFT data, which constrain this early part of the uplift history, are scattered, but also because our model set-up assumes step-function changes in the rock uplift rate. As such, a single model iteration cannot constrain a progressive slowdown in rock uplift. However, the Bayesian approach will capture a gradual slowdown as a widely distributed posterior in the transition time from one uplift rate to another. This behaviour can be visualized and quantified with the mean uplift history derived from the model ensemble. The progressive

slowdown is observed in the mean uplift path for each site and typically extends from ~25 to 15 Ma (Fig. 4a,b).

After this period, rock uplift rates are consistently low, and the mean rock uplift path at all sites drops between -11 and 8 Ma (Fig. 4). In Sila and Serre, rates fall to near zero, and in Aspromonte to -0.25 mm yr⁻¹ (Fig. 4). Higher rates in Aspromonte are expected as the southern tip of the Calabrian forearc side-swiped the northern tip of the African margin from -5 to 1.5 Ma, a process recorded in the geomorphology from north Sicily⁴². We interpret this north-south increase in uplift rate to be associated with localized crustal thickening along the southern tip of Calabria due to this glancing collision.

Rock uplift rates accelerate to ~0.5–1.0 mm yr⁻¹ at all sites between ~1.6 and 1.0 Ma, with faster rates in Aspromonte, ~0.9 mm yr⁻¹, and comparable rates in Sila and Serre, ~0.55–0.60 mm $yr^{\text{--}1}\text{(Fig.}4\text{a,b)}\text{.}$ Increased uplift rates first occur in Sila, then Aspromonte, and finally Serre, with best-fit timings of 1.6, 1.2 and 1.0 Ma, respectively (Fig. 4a,b). The differences in the timing and rate of this acceleration are reflected in the knickpoint elevations at ~1.0, 1.3 and 0.9 km in Sila, Aspromonte and Serre, respectively (Fig. 3). The abruptness of the onset, effectively a step function, and the diachronous uplift patterns are consistent with recent tearing of the Calabrian slab and opening of slab windows to the north and south of the modern-day forearc^{2,25}. Initiation of rapid uplift occurs above the torn slab segments, first in the north and then in the south, before affecting the centre of the forearc a few hundred thousand years later, perhaps facilitated by mantle flow around the torn slab edges^{2,25}. This event generated surface uplift and an isostatic response to enhanced erosion that partially sustains the high uplift rates in Calabria today (Extended Data Fig. 5).

Linking forearc uplift and long-term subduction dynamics

The uplift history for each site is remarkably consistent, demonstrating that the entire forearc responded similarly to geodynamic forcing. We

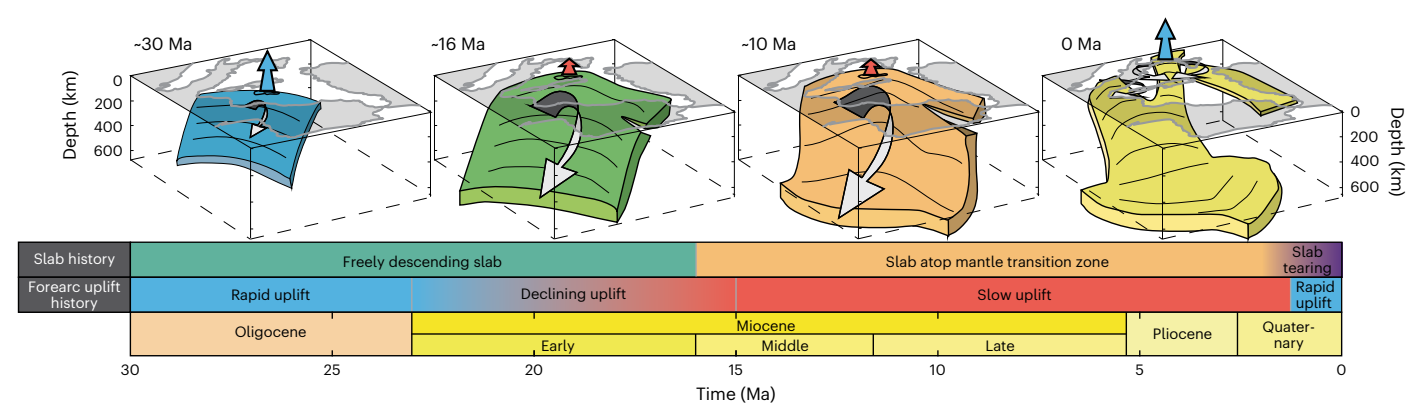


Fig. 5 | **Interpretive model for the impact of slab—mantle interactions on the upper plate.** Conceptual block model of the portion of the subducting slab through time (based on refs. 17,18,49). Vertical arrows represent rock uplift history from the inversion. The downward-directed grey arrows show the growing upper-mantle convection cell beneath the upper plate. The grey

arrows at 0 Ma show mantle flow around torn slab segments in Calabria, and the central Apennines are interpreted to disrupt the large upper-mantle convection cell. The lower bar shows show the slab descent history through time and the uplift history of Calabria, which is similar to other locations in the Italian peninsula (for context).

summarize the long-term rock uplift history as rapid to progressively declining from ~30 to 15 Ma, slow from ~15 to 1.5 Ma, and rapid from ~1.5 to 0 Ma, but acknowledge nuances, as discussed above (Fig. 4a,b).

The Mediterranean is a closing basin with a thick sedimentary cover where thicknesses on subducting oceanic lithosphere vary by a factor of only about two⁴¹. As such, the larger order-of-magnitude changes in subduction velocity will dominate accretionary flux variations, and positive correlations between subduction velocity and rock uplift are expected if the subduction wedge is controlled by crustal dynamics^{4–6}. Surprisingly, the rock uplift histories bear little resemblance to the subduction rate history and are clearly anticorrelated from 10 Ma to the present (Fig. 4b,c). We conclude that crustal accretion cannot explain Calabria's rock uplift history.

Changes in megathrust strength can affect forearc topography. Increased megathrust strength facilitates strong basal tractions, causing crustal thickening and uplift, and the opposite occurs if the plate interface weakens^{3,6,43}. Although several factors impact megathrust strength, over the long term, the amount of sediment entering the trench is thought to be an important factor, with more sediment equating to weaker plate interfaces^{43–45}. Subducting plates in the Mediterranean are covered with copious amounts of sediment⁴⁶, implying weak megathrusts through time. Thus, changes in plate interface strength seem an unlikely explanation for our results.

Numerical and analogue models of subduction demonstrate that slab-mantle interactions can affect upper plate topography throughout the lifetime of subduction 11-13. For retreating systems, models show that there are some adjustments to upper topography during the slab's free descent phase, where forearc elevations slightly decline. However, as the upper-mantle flow field induced by the descending slab begins to interact with the mantle transition zone, the upper-mantle convection cell strengthens, inducing long-wavelength trenchward tilting of the upper plate over several million years 11-13. The forearc is progressively pulled down during this period of slab-mantle interaction, and forearc elevations remain low after the slab rests atop the mantle transition zone.

Calabria's long-term rock uplift history appears consistent with these predictions from -25 to 1.5 Ma, where rock uplift rates begin to decline as the slab approaches the mantle transition zone, until the Middle-to-Late Miocene, when the slab drapes atop this boundary (Fig. 4a,b,d). Rock uplift rates then stay low, despite a large increase in subduction rate at -10 Ma, until slab fragmentation in the Quaternary. We infer that the abrupt increase in uplift rates beginning at 1.5 Ma is due to slab fragmentation. Slab tearing will induce an isostatic response

as the dense slab breaks apart. Furthermore, the newly torn slab can allow for small-scale lateral mantle flow around the torn slab edges, which probably disrupted the large upper-mantle convection cell (Fig. 4d). Within this view, Quaternary uplift in Calabria is not an anomaly, but is an expected response to slab fragmentation.

The -25–1.5-Ma period is perhaps the most intriguing part of Calabria's orogenic history. Based on existing geodynamic models, the observed behaviour can be linked to slab—mantle interactions and changes in the upper-mantle flow field; however, the exact forces and processes involved are not entirely understood^{11–13}. Future geodynamic modelling studies can potentially isolate the precise driving mechanisms in the context of our empirical dataset. Regardless of some remaining uncertainty, it is apparent that slab—mantle interactions are critical in understanding Calabria's rock uplift history.

The rock uplift history in Calabria, at least since the Middle Miocene, bears broad similarities to uplift and mineral cooling histories in the central and southern Apennines^{47,48}. Results from this portion of the Italian peninsula suggest slow uplift and slow cooling or reheating until -2–1 Ma, when uplift and exhumation rates accelerated. We suggest a common mechanism might explain the dynamics of the entire Italian peninsula (Fig. 5). A strong upper-mantle convection cell grew through time, dynamically suppressing elevations and rock uplift in the Italian peninsula by effectively counteracting isostasy until the Quaternary. Once the slab fragmented beneath Calabria and the Central Apennines, the convection cell was disrupted, and the peninsula uplifted rapidly due to changes in isostatic equilibrium and mantle dynamics (Fig. 5).

Conclusions

We have presented a continuous 30-Myr history of rock uplift for the Calabrian forearc. Our results show a consistent uplift history that does not resemble the subduction velocity history, suggesting that models of forearc growth by crustal accretion cannot explain our results. In the context of slab descent reconstructions and geodynamic models, our results imply that slab—mantle interactions control forearc rock uplift in Calabria. We infer that the forearc uplift was progressively depressed as the slab descended through the upper mantle, exciting a growing convection cell that held the upper plate down. After the slab draped over the mantle transition zone, the convection cell was established, and forearc rock uplift rates remained low. Once the slab fragmented in the Quaternary, small-scale mantle flow around torn slab edges disrupted the large upper-mantle convection cell. Destruction of the upper-mantle convection cell, along with isostatic changes associated with slab tearing, we argue, facilitated rapid uplift of Calabria

and probably other parts of the Italian peninsula since -2-1 Ma. Our approach and results have important implications for understanding the drivers of subduction orogenesis in the Mediterranean and elsewhere globally.

Online content

Any methods, additional references, Nature Portfolio reporting summaries, source data, extended data, supplementary information, acknowledgements, peer review information; details of author contributions and competing interests; and statements of data and code availability are available at https://doi.org/10.1038/s41561-023-01185-4.

References

- Willett, S. D. & Brandon, M. T. On steady states in mountain belts. Geology 30, 175–178 (2002).
- Faccenna, C. & Becker, T. W. Topographic expressions of mantle dynamics in the Mediterranean. *Earth Sci. Rev.* 209, 103327 (2020).
- Dielforder, A., Hetzel, R. & Oncken, O. Megathrust shear force controls mountain height at convergent plate margins. *Nature* 582, 225–229 (2020).
- Whipple, K. X. & Meade, B. J. Orogen response to changes in climatic and tectonic forcing. *Earth Planet. Sci. Lett.* 243, 218–228 (2006).
- Stolar, D. B., Willett, S. D. & Roe, G. H. in *Tectonics, Climate, and Landscape Evolution* Vol. 398 (eds Willett, S. D. et al.)
 Ch. 14 (Geological Society of America, 2006); https://doi.org/10.1130/2006.2398(14)
- Dahlen, F. A. Critical taper model of fold-and-thrust belts and accretionary wedges. Annu. Rev. Earth Planet Sci. 18, 55–99 (1990).
- Faccenna, C., Becker, T. W., Conrad, C. P. & Husson, L. Mountain building and mantle dynamics. *Tectonics* 32, 80–93 (2013).
- Faccenna, C., Oncken, O., Holt, A. F. & Becker, T. W. Initiation of the Andean orogeny by lower mantle subduction. *Earth Planet*. Sci. Lett. 463, 189–201 (2017).
- Faccenna, C. & Becker, T. W. Shaping mobile belts by small-scale convection. *Nature* 465, 602–605 (2010).
- Briaud, A., Agrusta, R., Faccenna, C., Funiciello, F. & van Hunen, J. Topographic fingerprint of deep mantle subduction. J. Geophys. Res. Solid Earth 125, e2019JB017962 (2020).
- Crameri, F. & Lithgow-Bertelloni, C. Abrupt upper-plate tilting during slab-transition-zone collision. *Tectonophysics* 746, 199–211 (2018).
- Cerpa, N. G. & Arcay, D. Overriding plate velocity control on surface topography in 2D models of subduction zones. *Geochem. Geophys. Geosyst.* 21, e2019GC008900 (2020).
- Xue, K., Schellart, W. P. & Strak, V. Overriding plate deformation and topography during slab rollback and slab rollover: insights from subduction experiments. *Tectonics* 41, e2021TC007089 (2022)
- Faccenna, C., Becker, T. W., Miller, M. S., Serpelloni, E. & Willett, S. D. Isostasy, dynamic topography and the elevation of the Apennines of Italy. *Earth Planet. Sci. Lett.* 407, 163–174 (2014).
- Glotzbach, C. Deriving rock uplift histories from data-driven inversion of river profiles. Geology 43, 467–470 (2015).
- Gallen, S. F. & Fernández-Blanco, D. A new data-driven Bayesian inversion of fluvial topography clarifies the tectonic history of the Corinth Rift and reveals a channel steepness threshold. J. Geophys. Res. Earth Surf 126, e2020JF005651 (2021).
- Faccenna, C., Jolivet, L., Piromallo, C. & Morelli, A. Subduction and the depth of convection in the Mediterranean mantle. J. Geophys. Res. Solid Earth 108, 2099 (2003).
- Goes, S. et al. A recent tectonic reorganization in the south-central Mediterranean. *Earth Planet. Sci. Lett.* 226, 335–345 (2004).

- Royden, L. H. Evolution of retreating subduction boundaries formed during continental collision. *Tectonics* 12, 629–638 (1993).
- Malinverno, A. & Ryan, W. B. F. Extension in the Tyrrhenian Sea and shortening in the Apennines as result of arc migration driven by sinking of the lithosphere. *Tectonics* 5, 227–245 (1986).
- Faccenna, C., Piromallo, C., Crespo-Blanc, A., Jolivet, L. & Rossetti, F. Lateral slab deformation and the origin of the western Mediterranean arcs. *Tectonics* 23, TC1012 (2004).
- van Dijk, J. P. & Scheepers, P. J. J. Neotectonic rotations in the Calabrian Arc; implications for a Pliocene-recent geodynamic scenario for the Central Mediterranean. *Earth Sci. Rev.* 39, 207–246 (1995).
- 23. Westaway, R. Quaternary uplift of southern Italy. J. Geophys. Res. Solid Earth 98, 21741–21772 (1993).
- Molin, P., Pazzaglia, F. J. & Dramis, F. Geomorphic expression of active tectonics in a rapidly-deforming forearc, Sila massif, Calabria, southern Italy. Am. J. Sci. 304, 559–589 (2004).
- Faccenna, C. et al. Topography of the Calabria subduction zone (southern Italy): clues for the origin of Mt. Etna. *Tectonics* 30, TC1003 (2011).
- Olivetti, V., Cyr, A. J., Molin, P., Faccenna, C. & Granger, D. E. Uplift history of the Sila Massif, southern Italy, deciphered from cosmogenic ¹⁰Be erosion rates and river longitudinal profile analysis. *Tectonics* 31, TC3007 (2012).
- Quye-Sawyer, J., Whittaker, A. C., Roberts, G. G. & Rood, D. H. Fault throw and regional uplift histories from drainage analysis: evolution of southern italy. *Tectonics* 40, e2020TC006076 (2021).
- Vignaroli, G., Minelli, L., Rossetti, F., Balestrieri, M. L. & Faccenna, C. Miocene thrusting in the eastern Sila Massif: implication for the evolution of the Calabria-Peloritani orogenic wedge (southern Italy). *Tectonophysics* 538–540, 105–119 (2012).
- 29. Cyr, A. J., Granger, D. E., Olivetti, V. & Molin, P. Quantifying rock uplift rates using channel steepness and cosmogenic nuclidedetermined erosion rates: examples from northern and southern Italy. *Lithosphere* **2**, 188–198 (2010).
- 30. Roda-Boluda, D. C., D'Arcy, M., Whittaker, A. C., Gheorghiu, D. M. & Rodés, Á. ¹⁰Be erosion rates controlled by transient response to normal faulting through incision and landsliding. *Earth Planet. Sci. Lett.* **507**, 140–153 (2019).
- Dumas, B., Guérémy, P., Lhénaff, R. & Raffy, J. Périodicités de temps long et de temps court, depuis 400,000 ans, dans l'étagement des terrasses marines en Calabre méridionale (Italie)/ Long and short timing from 400,000 years in the stepped marine terraces in Southern Calabria (Italy). Géomorphol. Reli. Process. Environ. 6, 25–44 (2000).
- Dumas, B. & Raffy, J. Enregistrement geomorphologique de maxima glacio-eustatiques dans la region soulevee de Soverato (Italie du sud). *Bull. Soc. Géol. Fr.* 167, 285–293 (1996).
- Dumas, B., Guérémy, P., Lhénaff, R. & Raffy, J. Morphometric reconstitution of a series of paleoshorelines in a dissected relief in Locride (Ionian Calabria, Italy). Geodin. Acta 8, 185–198 (1995).
- 34. Carobene, L. Genesi, età, sollevamento ed erosione dei terrazzi marini di Crosia-Calopezzati (Costa ionica della Calabria-Italia). *Alp. Mediterr. Quat.* **16**, 43–90 (2003).
- Cucci, L. Raised marine terraces in the Northern Calabrian Arc (Southern Italy): a ~600-kyr-long geological record of regional uplift. Ann. Geophys. 47, 1391–1406 (2004).
- 36. Ferranti, L. et al. Markers of the last interglacial sea-level high stand along the coast of Italy: tectonic implications. *Quat. Int.* **145–146**, 30–54 (2006).
- 37. Howard, A. D. A detachment-limited model of drainage basin evolution. *Water Resour. Res.* **30**, 2261–2285 (1994).
- Whipple, K. X. & Tucker, G. E. Dynamics of the stream-power river incision model: implications for height limits of mountain ranges,

- landscape response timescales and research needs. J. Geophys. Res. Solid Earth **104**, 17661–17674 (1999).
- 39. Whipple, K. X. Bedrock rivers and the geomorphology of active orogens. *Annu. Rev. Earth Planet Sci.* **32**, 151–185 (2004).
- 40. Sambridge, M. Geophysical inversion with a neighbourhood algorithm—I. Searching a parameter space. *Geophys. J. Int.* **138**, 479–494 (1999).
- 41. Kirby, E. & Whipple, K. X. Expression of active tectonics in erosional landscapes. *J. Struct. Geol.* **44**, 54–75 (2012).
- 42. Pavano, F. & Gallen, S. F. A geomorphic examination of the Calabrian forearc translation. *Tectonics* **40**, e2020TC006692 (2021).
- Beaumont, C., Ellis, S. & Pfiffner, A. Dynamics of sediment subduction-accretion at convergent margins: short-term modes, long-term deformation and tectonic implications. J. Geophys. Res. Solid Earth 104, 17573–17601 (1999).
- Kopf, A. & Brown, K. M. Friction experiments on saturated sediments and their implications for the stress state of the Nankai and Barbados subduction thrusts. *Mar. Geol.* 202, 193–210 (2003).
- 45. Tobin, H. J. & Saffer, D. M. Elevated fluid pressure and extreme mechanical weakness of a plate boundary thrust, Nankai Trough subduction zone. *Geology* **37**, 679–682 (2009).
- 46. Molinari, I. & Morelli, A. EPcrust: a reference crustal model for the European Plate. *Geophys. J. Int.* **185**, 352–364 (2011).

- 47. San Jose, M. et al. Stable isotope evidence for rapid uplift of the central Apennines since the late Pliocene. *Earth Planet. Sci. Lett.* **544**, 116376 (2020).
- 48. Fellin, M. G. et al. Transition from slab roll-back to slab break-off in the central Apennines, Italy: constraints from the stratigraphic and thermochronologic record. *GSA Bull.* **134**, 1916–1930 (2021).
- Faccenna, C., Becker, T. W., Lucente, F. P., Jolivet, L. & Rossetti,
 F. History of subduction and back arc extension in the Central Mediterranean. Geophys. J. Int. 145, 809–820 (2001).
- Maesano, F. E., Tiberti, M. M. & Basili, R. The Calabrian Arc: three-dimensional modelling of the subduction interface. Sci. Rep. 7, 8887 (2017).

Publisher's note Springer Nature remains neutral with regard to jurisdictional claims in published maps and institutional affiliations.

Springer Nature or its licensor (e.g. a society or other partner) holds exclusive rights to this article under a publishing agreement with the author(s) or other rightsholder(s); author self-archiving of the accepted manuscript version of this article is solely governed by the terms of such publishing agreement and applicable law.

@ The Author(s), under exclusive licence to Springer Nature Limited 2023

Methods

AFT and AHe measurements

We collected vertical transects of granite, gneiss and schist bedrock samples in the Serre Massif and the Aspromonte Massif from freshly exposed road cuts (Fig. 2d). In Serre, five samples span an elevation range from -180 m to 1,120 m above modern sea level, with an average vertical sample spacing of -150 m (Extended Data Table 1). In Aspromonte, we acquired six samples ranging in elevation from -530 m to 1,220 m, with a mean vertical spacing of -140 m. Bedrock samples were crushed, sieved and separated using standard magnetic and density separation techniques by GeoSep Services. For each transect, all samples were analysed for AHe (Source Data Fig. 2d), and samples representing the lowest, highest and a central elevation were used in AFT analysis (Source Data Fig. 2c).

AFT. We conducted AFT analyses at GeoSep Services using standard techniques for laser-ablation inductively coupled plasma mass spectrometry. Following ref. 51, apatite grains were mounted in an epoxy resin that was cured for 4 h at 90 °C. The mounts were ground and polished to expose the internal grain surface. Samples were etched in 5.5 N HNO₃ for 20.0 ± 0.5 s at 21 ± 1 °C to reveal naturally occurring fission tracks. Spontaneous tracks were counted on the grain mounts in unpolarized light at ×2,000 magnification. Regions on individual grains where the spontaneous tracks were counted were analysed by laser-ablation inductively coupled plasma mass spectrometry to determine the ²³⁸U concentrations from measurements of the ²³⁸U to ⁴³Ca ratio. Single-grain dates were calculated using the ratio of the density of natural fission tracks in the grain to the amount of ²³⁸U present and a modified version of the radioactive decay equation that includes a zeta calibration factor⁵¹. We include all grains with zero spontaneous tracks in the counted area to ensure the data were unbiased. Forty single-grain analyses were used to calculate sample ages, and pooled fission track ages were used.

We obtained track length distribution data following age analysis. Samples were irradiated with a ²⁵²Cf source in a vacuum chamber to enhance the number of confined tracks available for measurement⁵¹. Grains were re-etched as above to illuminate horizontal, confined fission tracks. Only natural, horizontal, confined fission tracks with clearly visible ends were measured, in unpolarized light at ×2,000 magnification. The length and crystallographic orientation of each track was measured using a digitizing tablet with a personal computer. The precision of each track length was approximately $\pm 0.20 \,\mu m$, and the precision of the track angle relative to the crystallographic c axis was $\sim \pm 2^{\circ}$. For either AFT age or confined track length determination, kinetic information (Dpar) was acquired for each grain. Dpar is defined as the fission track etch pit diameter parallel to the crystallographic c axis at the polished grain surface. For grains with zero tracks, Dpar was measured in a different area that contained tracks but was not near a cracked or pitted feature or close to the grain boundary.

AHe. We conducted (U-Th)/He analyses at the University of Texas UTChron Laboratory using standard procedures (https://www.jsg.utexas.edu/utchron-lab/u-th-he-lab/). Individual apatite grains were screened for quality, size, shape and inclusions using a binocular microscope at ×180 magnification. Four to eight single-grain aliquots were measured per sample. Individual aliquots were photographed and measured for standard geometric alpha-ejection age (Ft) corrections. The selected grains were characterized by an average equivalent spherical radius of 45.3 µm and a corresponding Ft value of 0.66. Each single-grain apatite aliquot was wrapped in platinum foil tubes, laser heated for 5 min at 1,070 °C, analysed for He, and reheated to ensure complete degassing. After degassing, radiogenic He was analysed in an all-metal, automated ultrahigh-vacuum He extraction line with precision volume aliquot systems for ³He isotope dilution and delivery of ⁴He standard gas, a cryogenic gas purification system, and a Balzers Prisma QMS-200

quadrupole mass spectrometer for measuring 3 He/ 4 He ratios. This procedure allows for very low blank and high-precision He measurements (-0.3–0.5%). After complete degassing, aliquots were retrieved and dissolved for U, Th and Sm measurements. Samples were spiked (235 U, 230 Th and 149 Sm) and dissolved in 30% HNO $_3$ at 90 °C for 1 h. Aliquot solutions were analysed for U, Th and Sm using a Thermo Element2 HR-ICP-MS fitted with a CETAC micro-concentric nebulizer and ESI autosampler. The data were then compiled and reduced using an in-house custom visual-basic Excel add-in macro.

All analytical uncertainties were captured and propagated during the multi-step, multi-instrument AHe analysis. Analytical uncertainties including He and (U, Th, Sm) measurement errors were -0.3–0.5% and <1–2%, respectively. Alpha-ejection corrections are more challenging to quantify due to assumptions of homogeneous U and Th distributions and result in propagated analytical uncertainties that generally underestimate aliquot reproducibility. In an effort to better represent the 'true' uncertainty, a percentage error is commonly assigned to an aliquot analysis based on the standard deviation of a population derived from standard samples, which is 6% for apatite in the UTChron laboratory. Mean ages for individual samples were calculated from all single-grain ages for individual samples.

Empirical calibration of the stream power model

To obtain an idea of reasonable priors for the stream power parameters, we conducted an analysis of digital fluvial topography and ¹⁰Be-derived basin average concentration data. We compiled all published basin average ¹⁰Be measurements from Calabria^{26,29,30} (n = 36; Supplementary Table 2). We recalculated erosion rates for each basin to standardize the compilation using the approach of ref. 52. This procedure assumes sediments are well-mixed and corrects measured ¹⁰Be concentrations using the depth-, latitude- and altitude-dependent spallogenic and muonic production rates of refs. 53,54 to determine the average erosion rate in the catchment. A Monte Carlo routine was used to propagate uncertainties in the measured nuclide concentrations and other model parameters (details are provided in ref. 52). Following ref. 55, we did not apply a shielding correction.

We used TopoToolbox v2 and ChiProfiler for topographic and river profile analysis^{56,57}. We used an ~30-m horizontal resolution shuttle radar topography mission DEM to fill sinks, determine flow directions and calculate the upstream accumulation area for the entire landscape. We defined the river network as all areas draining more than 1 km². Using the χ-dispersion approach 58,59, we determined the empirical concavity index, ~0.40, for rivers draining over metamorphic and igneous rock units. For all basins with a ¹⁰Be measurement, we delineated the drainage basins and river networks and calculated the transformed distance coordinate χ , which is the path integral of the inverse of drainage area raised to the empirically derived concavity index⁶⁰. The normalized steepness index, $k_{\rm sn}$, is a stream channel metric that normalizes local channel slope to upstream drainage area, allowing for comparison of channel steepness at different drainage areas⁴¹. We determined the basin average k_{sn} based on a regression of χ -elevation data and used the approach of ref. 61 to determine uncertainties accounting for the autocorrelation of residuals (Supplementary Table 2).

From the 10 Be-derived erosion rates and the basin average $k_{\rm sn}$ data, we empirically calibrated the stream power model (details for this model are provided in the next section) based on the following relationship:

$$E = Kk_{\rm sn}^n,\tag{2}$$

where E is the basin average erosion rate, K is the erodibility constant, and n is the slope exponent in the stream power model¹⁶. We used a total least-squares regression through log-transported E and $K_{\rm sn}$ data to determine reasonable values for E and E0, excluding one outlier in the data (Extended Data Fig. 4). The empirical concavity index, which

is equal to the ratio of the drainage area exponent, m, and the slope exponent, n, in the stream power model, was used to estimate m based on the results from the regression. We used a Monte Carlo routine to propagate the uncertainties in the regression and found that n is -1.30 and K is -3.34 × 10⁻⁶ m^{1-2m} yr⁻¹. Based on this analysis, we conservatively assign priors on the stream power model that ranged from 1.0 to 1.5 to cover the full range of the data (Extended Data Fig. 4). We note that when n > 1, some parts of the uplift history recorded in the river profiles might be erased with an increase in uplift rate 62 ; however, the data-driven approach used here lessens the likelihood of this information loss 16 . The m to n ratio is allowed to range between 0.3 and 0.7, n from 1.0 to 1.5 and K from 1 × 10⁻⁸ to 1 × 10⁻⁵ m^{1-2m} yr⁻¹.

Forward models

We applied a series of forward models to predict the topographic and analytical data given an input rock uplift history. We used the stream power model to predict the river network elevations and erosion history, given a rock uplift history. We then used the output topographic and erosion history to drive (1) thermal and kinetic models that predict low-temperature thermochronology data, (2) cosmogenic nuclide production and attenuation models to predict ¹⁰Be concentrations and (3) a simple model for recent rock uplift to compare to marine terrace-derived rock uplift results. The forward and inverse model here are based on those presented in ref. 15, with some minor modifications.

Stream power model. This detachment-limited stream power model (equation (1)) model can be used to simulate the evolution of a river profile through time when placed into a continuity equation with rock uplift, *U*:

$$\frac{\mathrm{d}z}{\mathrm{d}t} = U(x, t) - KA(x)^m S(x, t)^n \tag{3}$$

where z is elevation, t is time, and x is streamwise distance. Because we are working on the small-to-moderate catchment scale, we assumed that spatial variations in *U* are negligible. We assumed the drainage area had not changed substantially over time. Although it is impossible to evaluate this assumption over the long timescales considered, this assumption is reasonable over geologically recent timescales. Furthermore, the earlier portion of the uplift history determined by the thermochronological data is largely insensitive to drainage area, and the exact erosion rule used. The period where constant drainage area becomes important is for the simulated cosmogenic nuclide concentrations and river profile elevations. As such, we used the modern-day river network as defined by the shuttle radar topography mission DEM, resampled to 100 m to improve computational speed, to define A and x. We used an implicit finite-difference solver 63 to simulate the evolution of the river profiles using a 1,000-yr timestep in all models, which is a slight modification of the solver used in ref. 15.

The river network is assumed to be in a steady state with the initial uplift condition and selected stream power parameters and changes in response to temporal variations in rock uplift rate. From this starting condition, the river network for each catchment is allowed to evolve based on the assumed uplift history and the stream power parameters selected from the prior probability distributions. For a given rock uplift history, the model outputs are the erosion and topographic history of the river profile.

Thermal and kinetic models. The output topographic and erosion history from the stream power model was used to run thermal and kinetic models that predict the low-temperature thermochronology data. The one-dimensional heat-transfer equation was solved numerically using a finite-difference approach with standard thermal parameters (thermal diffusivity = 1×10^{-6} m² s⁻¹, heat production = 9.6×10^{-10} W kg⁻¹, crustal density = 2,700 kg m⁻³ and specific heat capacity = 800 J kg⁻¹K⁻¹).

Heat production was assumed to be temporally stable and decrease exponentially with depth, reaching an e-fold decline at 10-km depth. The upper thermal boundary condition was calculated with an atmospheric lapse rate of 5 °C km $^{-1}$, a sea-level temperature of 20 °C and the elevation history of the sample location. The basal boundary condition was set at 30-km depth for all models and determined by assuming an initial geothermal gradient of 25 °C km $^{-1}$, which was solved for in the model (for example, 25 °C km $^{-1}$ equates to 750 °C at 30-km depth). This inferred geothermal gradient is generally consistent with modern surface heat-flow measurements in southern Italy 64 , assuming typical thermal conductivities for higher-grade metamorphic and granitic rocks typical of Calabria.

Extracted time-temperature paths from the thermal model were used to calculate AHe ages, AFT ages and spontaneous track length distributions. The AHe data were simulated using the helium diffusion kinetics from RDAAM⁶⁵. The AFT data were modelled using the annealing model of ref. 66.

Cosmogenic nuclide model. The cosmogenic nuclide concentrations for 10 Be were modelled based on the last 2 Myr of the topographic and erosion history derived from the stream power model. This timescale ensures that the cosmogenic concentrations are integrated from a depth of several tens of metres to the surface. Site-specific concentrations were predicted as a function of the erosion history and the depth-, latitude- and altitude-dependent spallogenic ($P_{\rm sp}$) and muonic (P_{μ}) production rates of refs. 53,54:

$$N(h) = (N(h-1) + (P_{\rm sp}(h) + P_{\mu}(h)) dt) e^{-\lambda dt}$$
(4)

where N(h) is the nuclide concentration at depth below the surface, h, λ is the 10 Be decay constant, and dt is the timestep of the integration, here 100 yr in all calculations. Basin average concentrations, \bar{N} , were determined based on the average of all upstream concentrations:

$$\bar{N} = \frac{1}{n} \sum_{i=1}^{n} (E_{ij,t=0} N_{ij,z=0})$$
 (5)

where $E_{ij,t=0}$ is the erosion rate at node ij, and $N_{ij,z=0}$ is the corresponding 10 Be surface concentration at the end of the model run.

Marine terrace rock uplift. From the coastline near each catchment, we used published marine terrace inner shoreline elevations and inferred or measured ages³¹⁻³⁶ to calculate total rock uplift rates using a global sea-level curve⁶⁷ (Supplementary Table 3). For each site, we selected the most prominent set of terraces reported in each publication and selected the smoothest and simplest (that is, linear) uplift history for each site based on the reported elevations, inferred or measured terrace ages, and the timing and elevation of sea level at the time of terrace formation. We assumed that terraces were cut during periods of relative sea-level stability when rock uplift and sea-level rise rates were comparable and that terraces were abandoned at the end of a relative sea-level highstand^{23,36}. This simplifying assumption allowed us to correlate terraces to the timing and elevation of sea-level highstands to find the simplest uplift history possible, which we assumed is near linear.

Marine terraces were mapped near the outlet of the study catchments in Sila and Aspromonte, but we did not find published results near the outlet in Serre. Two studies published results to the north and south of the study catchment in Serre, and we combined these data to approximate the rock uplift here. We used a Monte Carlo routine to propagate uncertainties in the rock uplift rate calculation on the basis of reported uncertainties in the inner shoreline elevation, the sea-level elevation at the time of terrace formation, the timing of the sea-level highstand, and the geochronologic age, if available. The uncertainties used for this procedure are intentionally large for the

elevation and timing of each sea-level highstand to encompass the full range of uncertainty associated with different sea-level curves (for example, ref. 68; Supplementary Table 3). The derived rock uplift rates in Aspromonte, Serre and Sila are $-0.92~\rm mm~yr^{-1}$, $-0.63~\rm mm~yr^{-1}$ and $-0.88~\rm mm~yr^{-1}$, respectively. In our inversion, we sought to model the total rock uplift calculated from the marine terraces. To this end, we simply multiplied the inferred marine terrace age by the final uplift rate in the model to generate predictions of total rock uplift that could be compared to the marine terrace rock uplift values.

The inverse model

The inverse model uses the neighbourhood algorithm, which is an efficient Markov chain Monte Carlo sampler⁴⁰. The algorithm works by running a series of forward models that predict observed data. The model parameters first prescribe a possible range in the solution space based on prior knowledge, called the prior probability distributions ('the priors'). Here we assumed uniform priors about a range for each parameter. The x axis of the plots in Extended Data Figs. 1-3 represents the priors used for each parameter in this study, which are also presented in Extended Data Table 1. The algorithm populates the posterior probability distributions ('the posteriors') that represent the acceptable solution space using an optimized search algorithm. The search algorithm is guided by the priors, the quality of the model fit to the data, and the probability of transitioning from one position to another in the parameter space. The quality of fit ('misfit') between the observed and modelled data is defined as a Gaussian log-likelihood function $(\log(L))$:

$$\log(L) = -\sum_{i=1}^{n} \frac{\log(2\pi)}{2} + \log(\sigma_i) + 0.5 \left(\frac{\sigma_i - p_i}{\sigma_i}\right)^2$$
 (6)

where p_i is the predicted value (for example, river profile elevation, thermochronometric age, nuclide concentration, marine terrace elevation), o_i and o_i are the corresponding observed value and 1σ error, and n is the total number of observations. Each data type (the river profile, cosmogenic, marine terrace and thermochronology data) is given equal weight in the likelihood function. We initially ran a series of models for each site that initiate anywhere within the range of priors. From these models, we identified the highest-likelihood zone within the parameter space and started subsequent simulations from this high-likelihood zone, as is common practice with Markov chain Monte Carlo samplers to avoid searching in low-likelihood zones of the parameter space. We then aggregated all model results and used a likelihood threshold, defined as the 50th likelihood percentile, to define acceptable fits, which were used to populate the posterior probability distributions (Extended Data Figs. 1–3).

Data availability

Additional data used in this paper can be found in the publications and sources cited in the main text and Methods and the Extended Data and Source Data tables provided. The apatite fission track and apatite (U-Th/He) data generated and analysed in this study are archived in the following publicly available figshare data repositories: https://doi.org/10.6084/m9.figshare.22305889.v1 (apatite fission track) and https://doi.org/10.6084/m9.figshare.22305907.v1 (apatite (U-Th/He)). Source data are provided with this paper.

Code availability

Modified versions of the codes used in this study are available at https://github.com/sfgallen/RICoTTa and archived as a Zenodo repository at https://doi.org/10.5281/zenodo.7671209.

References

51. Donelick, R. A., O'Sullivan, P. B. & Ketcham, R. A. Apatite fission-track analysis. *Rev. Miner. Geochem.* **58**, 49–94 (2005).

- 52. Lupker, M. et al. ¹⁰Be-derived Himalayan denudation rates and sediment budgets in the Ganga basin. *Earth Planet. Sci. Lett.* **333–334**, 146–156 (2012).
- 53. Stone, J. O. Air pressure and cosmogenic isotope production. *J. Geophys. Res. Solid Earth* **105**, 23753–23759 (2000).
- Braucher, R. et al. Determination of muon attenuation lengths in depth profiles from in situ produced cosmogenic nuclides. Nucl. Instrum. Methods Phys. Res B Beam Interact. Mater. At. 294, 484–490 (2013).
- 55. DiBiase, R. A. Short communication: increasing vertical attenuation length of cosmogenic nuclide production on steep slopes negates topographic shielding corrections for catchment erosion rates. *Earth Surf. Dyn.* **6**, 923–931 (2018).
- Schwanghart, W. & Scherler, D. Short communication: TopoToolbox 2 – MATLAB-based software for topographic analysis and modeling in Earth surface sciences. *Earth Surf. Dynam.* 2, 1–7 (2014).
- Gallen, S. F. & Wegmann, K. W. River profile response to normal fault growth and linkage: an example from the Hellenic forearc of south-central Crete, Greece. Earth Surf. Dyn. 5, 161–186 (2017)
- Goren, L., Fox, M. & Willett, S. D. Tectonics from fluvial topography using formal linear inversion: theory and applications to the Inyo Mountains, California. J. Geophys. Res. Earth Surf. 119, 1651–1681 (2014).
- Gailleton, B., Mudd, S. M., Clubb, F. J., Grieve, S. W. D. & Hurst, M. D. Impact of changing concavity indices on channel steepness and divide migration metrics. J. Geophys. Res. Earth Surf. 126, e2020JF006060 (2021).
- 60. Perron, J. T. & Royden, L. An integral approach to bedrock river profile analysis. *Earth Surf. Process Landf.* **38**, 570–576 (2013).
- 61. Gallen, S. F. Lithologic controls on landscape dynamics and aquatic species evolution in post-orogenic mountains. *Earth Planet. Sci. Lett.* **493**, 150–160 (2018).
- Royden, L. & Taylor Perron, J. Solutions of the stream power equation and application to the evolution of river longitudinal profiles. J. Geophys. Res. Earth Surf. 118, 497–518 (2013).
- Braun, J. & Willett, S. D. A very efficient O(n), implicit and parallel method to solve the stream power equation governing fluvial incision and landscape evolution. Geomorphology 180–181, 170–179 (2013).
- 64. Vedova, B. D., Bellani, S., Pellis, G. & Squarci, P. in Anatomy of an Orogen: the Apennines and Adjacent Mediterranean Basins (eds Vai, G. B. & Martini, I. P.) 65–76 (Springer, 2001).
- 65. Flowers, R. M., Ketcham, R. A., Shuster, D. L. & Farley, K. A. Apatite (U–Th)/He thermochronometry using a radiation damage accumulation and annealing model. *Geochim. Cosmochim. Acta* 73, 2347–2365 (2009).
- Ketcham, R. A., Donelick, R. A. & Carlson, W. D. Variability of apatite fission-track annealing kinetics: III. Extrapolation to geological time scales. Am. Mineral. 84, 1235–1255 (1999).
- Waelbroeck, C. et al. Sea-level and deep water temperature changes derived from benthic foraminifera isotopic records. Quat. Sci. Rev. 21, 295–305 (2002).
- de Gelder, G. et al. How do sea-level curves influence modeled marine terrace sequences? Quat. Sci. Rev. 229, 106132 (2020).

Acknowledgements

This research was supported by Colorado State University startup funds and NSF award EAR-2041910 to S.F.G. and NSF PF award EAR-1952764 to N.M.S. We thank R. Chatterjee and D. Patterson (UT Chron facilities) for analytical support, J. Eidmann and E. Marder for field assistance, and D. Hill, M. Windingstad, N. Weaver and R. Forrey for laboratory assistance. We also thank L. Husson for insightful, constructive comments on an earlier version of this paper.

Author contributions

S.F.G. and N.M.S. conceived of the study and collected the thermochronometry samples presented. P.O. conducted the mineral separations and fission track analyses, and D.F.S. performed the noble gas thermochronometry measurements. C.G. provided the original inversion code. S.F.G. revised the codes and led the analysis with additional support from C.G. and N.M.S. S.F.G. drafted the figures and wrote the paper with input and feedback from all authors throughout the process.

Competing interests

The authors declare no competing interests.

Additional information

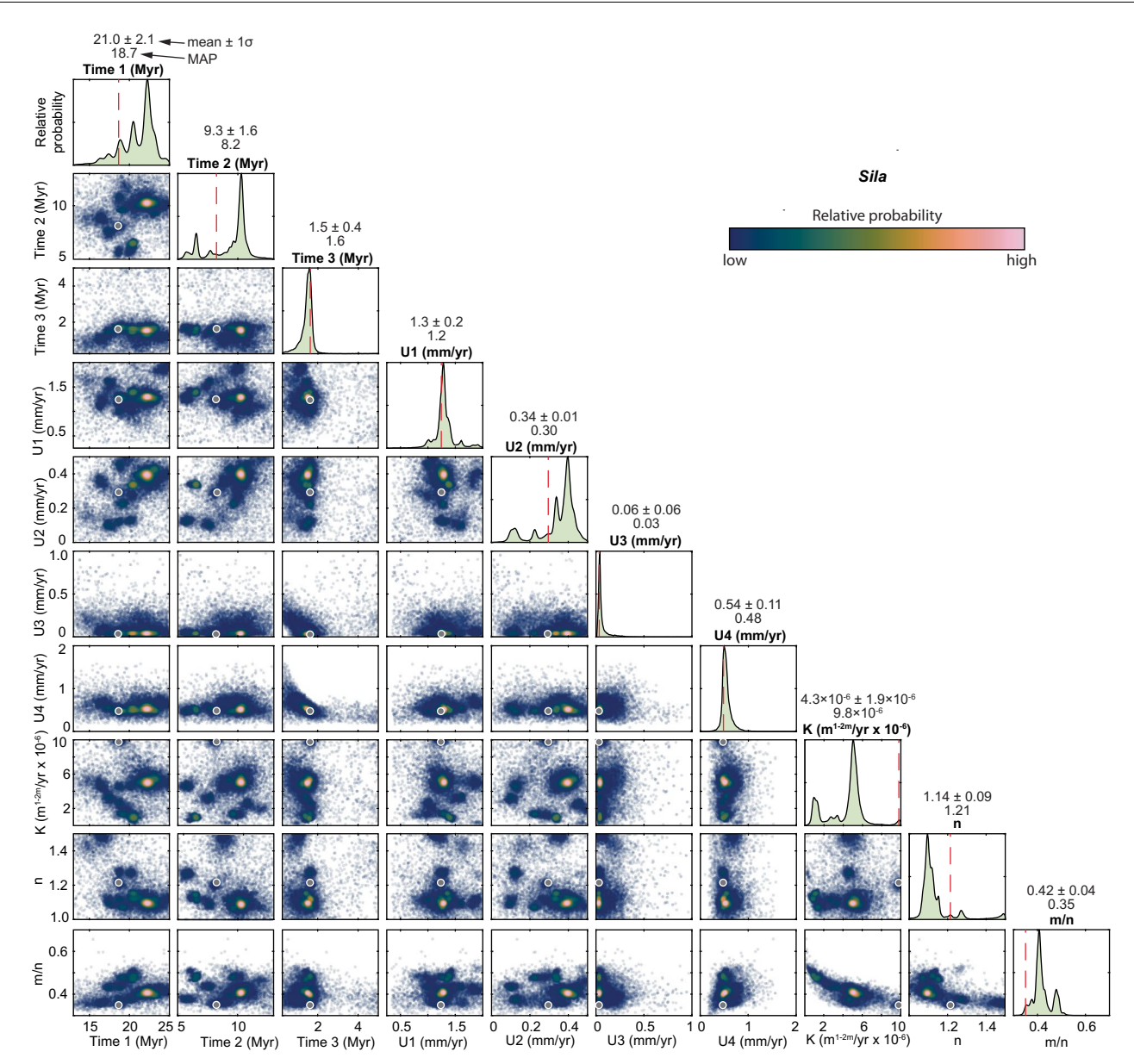
Extended data is available for this paper at https://doi.org/10.1038/s41561-023-01185-4.

Supplementary information The online version contains supplementary material available at https://doi.org/10.1038/s41561-023-01185-4.

Correspondence and requests for materials should be addressed to Sean F. Gallen.

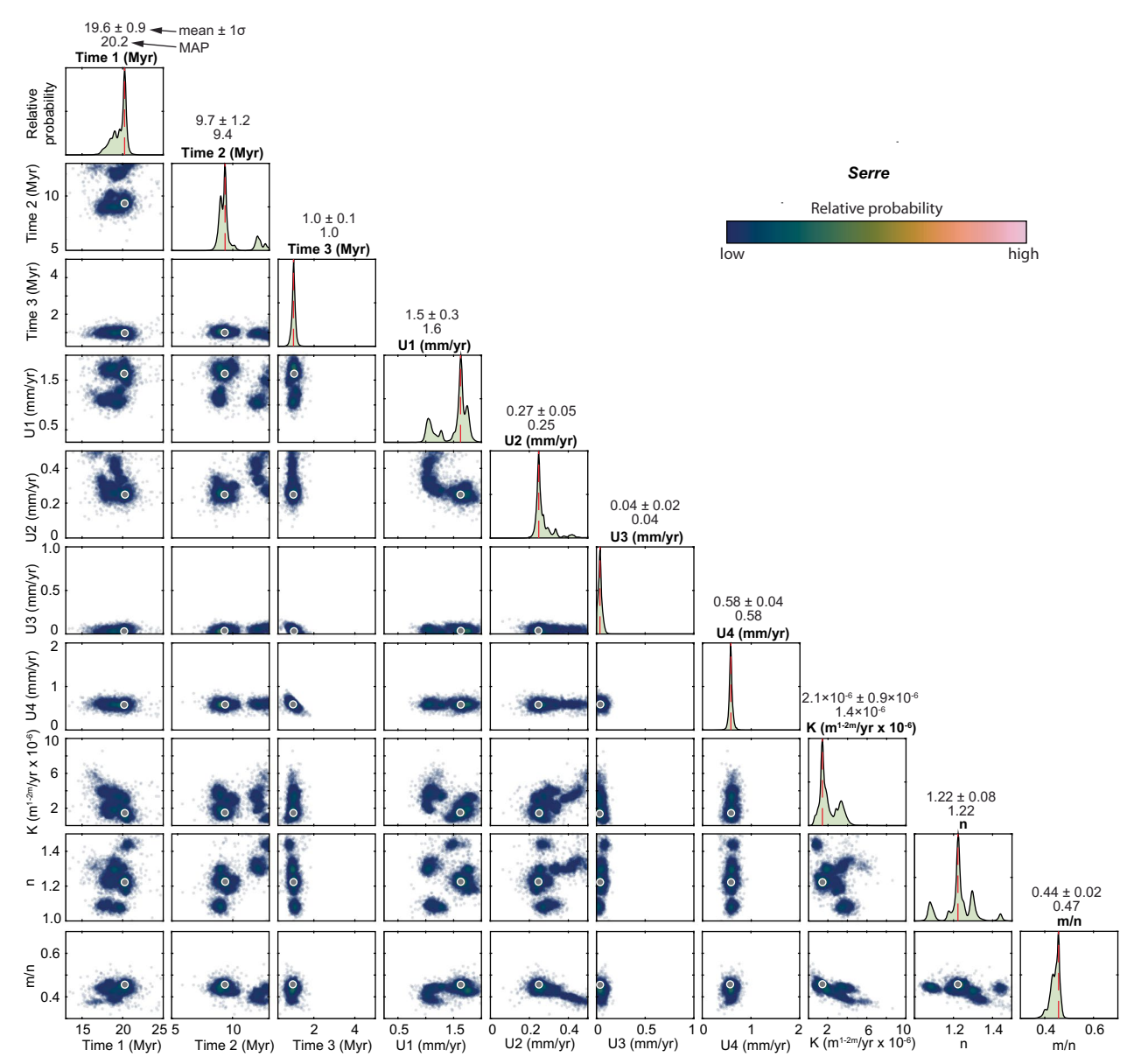
Peer review information *Nature Geoscience* thanks Laurent Husson, Magdalena Curry, Jean Braun and the other, anonymous, reviewer(s) for their contribution to the peer review of this work. Primary Handling Editor: Louise Hawkins, in collaboration with the *Nature Geoscience* team.

Reprints and permissions information is available at www.nature.com/reprints.

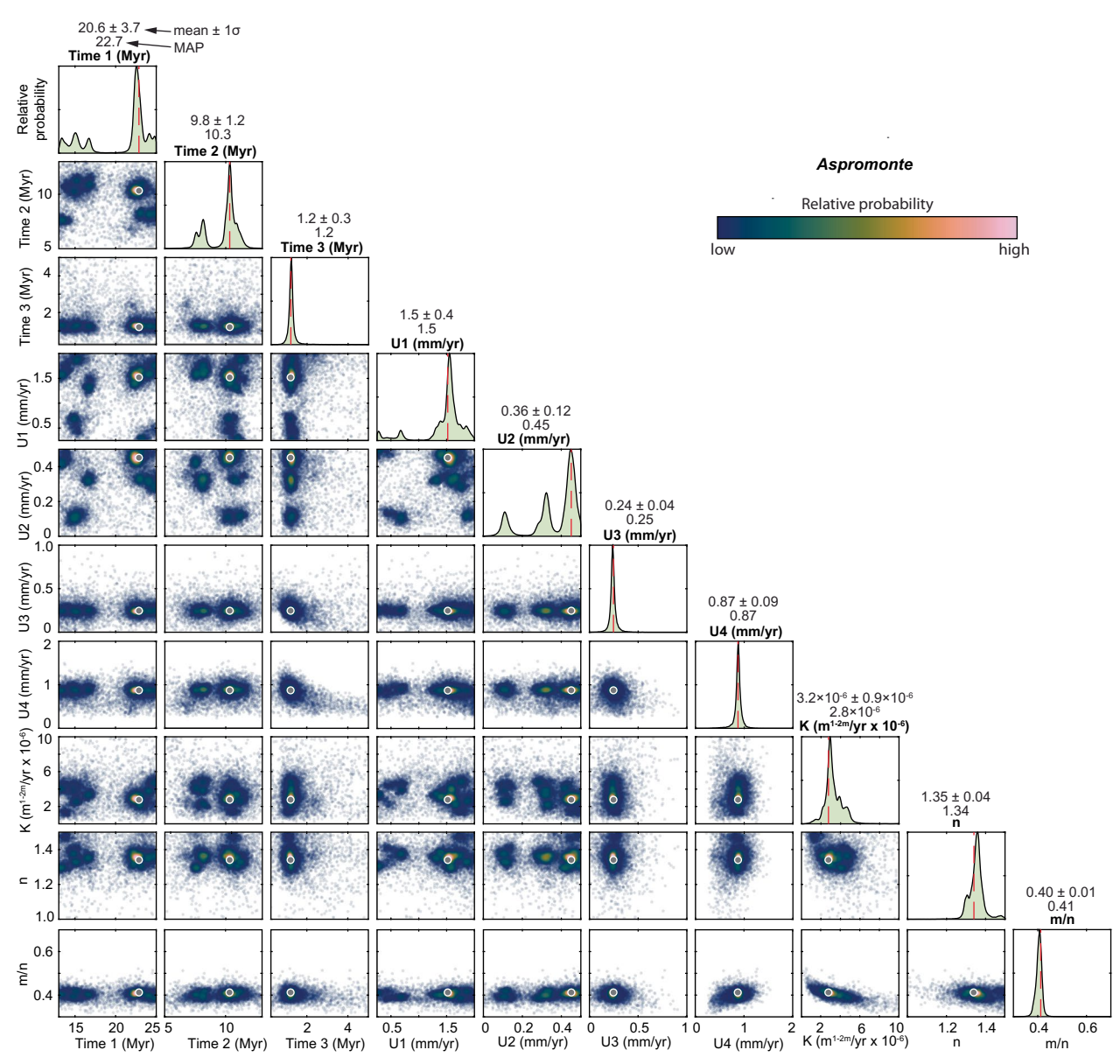


Extended Data Fig. 1| **Matrix plot of the posterior probability distributions** from the inversion of the catchment in the Sila massif. The probability density plots show the marginal posteriors and bivariate plots show the locations sampled during the inversion colored by their relative probability. The dashed red line in the marginal posterior plots and gray dot in the bivariate plots show the location of the maximum a posteriori (MAP) solution. Note that the points in the bivariate plots are transparent such that areas sampled more frequently

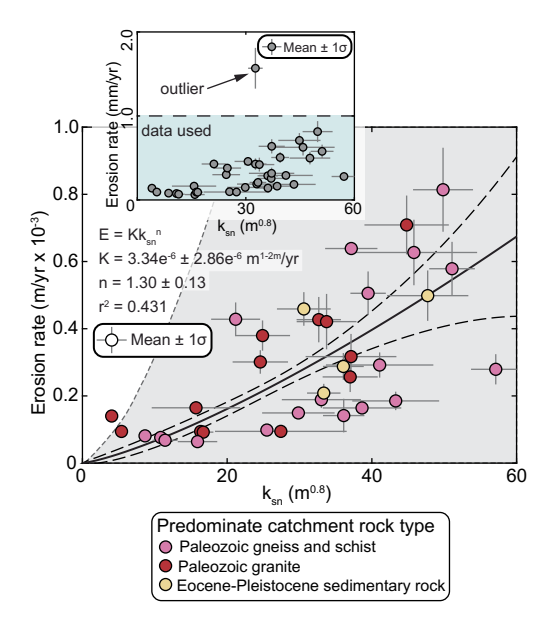
appear more opaque. Time 1 – transition from first to the second phase of uplift, Time 2 – transition from the second to the third phase of uplift, Time 3 – transition from the third to the fourth phase of uplift, U1 – initial uplift rate, U2 – second phase uplift rate, U3 – third phase uplift rate, U4 – final phase uplift rate, K – stream power erodibility constant, n stream power slope exponent, m/n – stream power m to n ratio.



Extended Data Fig. 2 | Matrix plot of the posterior probability distributions from the inversion of the catchment in the Serre massif. Same as in Extended Data Fig. 1, except the results are for the catchment in the Serre massif.

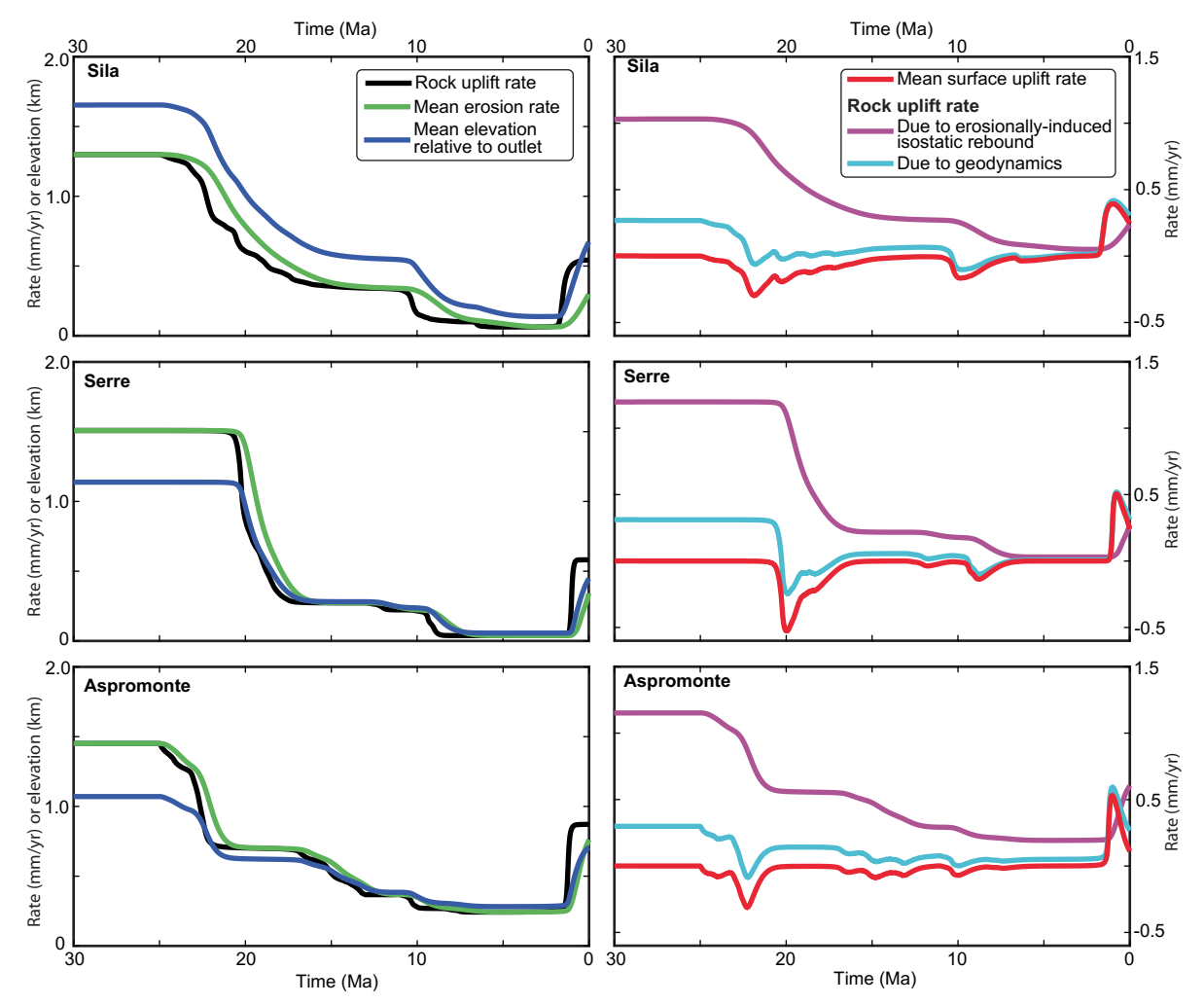


Extended Data Fig. 3 | **Matrix plot of the posterior probability distributions from the inversion of the catchment in the Aspromonte massif.** Same as in Extended Data Fig. 1, except the results are for the catchment in the Aspromonte massif.



Extended Data Fig. 4 | **Empirical calibration of the stream power model.** Plot showing the relationship between 10 Be-derived basin average erosion rates and basin average normalized steepness index, k_{sn} , for all basins in Calabria with published data. The inset shows all data and the main figure shows the dataset excluding one outlier. The solid black line and dashed black lines show the best-fit power-law regression through data using a total least-squares regression

and the one standard deviation uncertainties, respectively, from a Monte Carlo error propagation routine. The equation, best-fit parameters and associated one standard deviation uncertainties are shown along with the $\rm r^2$ value. The gray shaded region bound by the dashed gray line shows the range of stream power parameters searched in the inversion.



Extended Data Fig. 5 | Uplift, erosion, and elevation histories of catchments. The left column shows the mean rock uplift rate from the model ensemble from Fig. 4 and the mean erosion rate and the mean catchment elevation determined using the mean uplift rate history and the best-fit stream power parameters from the inversion. The right column shows the mean surface uplift rate from each catchment, determined as the difference between the rock uplift rate and the mean erosion rate from the left panel. The right column also shows the rock

uplift rate partitioned into isostatic and geodynamic components assuming Airy isostasy and typical crustal and mantle densities of $2700\,\mathrm{kg}\,\mathrm{m}^{-3}$ and $3400\,\mathrm{kg}\,\mathrm{m}^{-3}$, respectively. Note that the assumption of Airy isostasy is likely to overestimate the true contribution of erosion to rock uplift and underestimate the geodynamic component to rock uplift because it ignores lithospheric rigidity, which at the scales considered is non-negligible.

Extended Data Table 1 | List of Parameters Solved for in the Inverse Model with Range of Priors and Explanations

Symbol	Description	Units	Prior	Explanation
Stream power parameters				
К	Erodibility	m ^{1-2m} /yr	1×10^{-8} - 1×10^{-5}	Based on analysis of normalized steepness indices and basin average erosion rates from Calabria (Figure ED4)
n	Slope exponent		1.0 - 1.5	Based on analysis of normalized steepness indices and basin average erosion rates from Calabria (Figure ED4)
m/n	Ratio of the drainage area, m, and the slope exponent, n		0.3 - 0.7	Typically accepted range of values from the literature ^{15,26,40,43} and based on analysis of river profiles in Calabria
Rock uplift parameters				
U1	Initial uplift rate	mm/yr	0.25 - 2	Sila massif experienced a large amount of exhumation in the Early to Middle Miocene (ref. ²⁸)
Time1	Timing of the transition from U1 to U2	Ma	25 - 13	Forearc uplift rate is hypothesized to have slowed in the Miocene to bevel presently preserved relict
U2	Second phase uplift rate	mm/yr	0 - 0.5	topography ^{24,26} .
Time2	Timing of the transition from U2 to U3	Ma	13 - 5	Subduction velocity increases in the mid-to-late
U3	Third phase uplift rate	mm/yr	0 - 1.0	Miocene ^{17,29} and might affect forearc rock uplift rate.
Time3	Timing of the transition from U3 to U4	Ma	5 - 0.25	Rock uplift rate increased geologically recently,
U4	Final uplift rate	mm/yr	0 - 2	elevating relict topography, forming knickpoints, and preserving Pleistocene marine terraces ^{23,24,26,27}